Article

Seaweed-Liked WS$_2$/rGO Enabling Ultralong Cycling Life and Enhanced Rate Capability for Lithium-Ion Batteries

Yi Huang [1] , **Yu Jiang** [1] , **Zhaofei Ma** [1] , **Yan Zhang** [1] , **Xianfeng Zheng** [1] , **Xuemin Yan** [1,*] , **Xiaoqing Deng** [1] , **Wei Xiao** [1] **and Haolin Tang** [2,*]

[1] College of Chemistry and Environmental Engineering, Yangtze University, Jingzhou 434023, China; h-uangy-i@163.com (Y.H.); librajiangyu@163.com (Y.J.); libramzf@163.com (Z.M.); YanZhang@126.com (Y.Z.); XianfengZheng@126.com (X.Z.); XiaoqingDeng@126.com (X.D.); WeiXiao@126.com (W.X.)

[2] State Key Laboratory of Advanced Technology for Materials Synthesis and Processing, Wuhan University of Technology, Wuhan 430070, China

* Correspondence: XueminYan@126.com (X.Y.); thln@whut.edu.cn (H.T.); Tel.: +86-0716-806-0286 (X.Y.); +86-0716-806-0650 (H.T.)

check for updates

Abstract: WS$_2$ is considered as a potential anode material for lithium ion batteries (LIBs) with superior theoretical capacity and stable structure with two-dimensional which facilitates to the transportation and storage of lithium ion. Nevertheless, the commercial recognition of WS$_2$ has been impeded by the intrinsic properties of WS$_2$, including poor electrical conductivity and large volume expansion. Herein, a seaweed-liked WS$_2$/reduced graphene oxide (rGO) composites has been fabricated through a procedure involving the self-assembling of WO$_4^{2-}$, hexadecyl trimethyl ammonium ion with graphene oxide (GO) and the subsequent thermal treatment. The WS$_2$/rGO nanocomposite exhibited the outstanding electrochemical property with a stable and remarkable capacity (507.7 mAh·g^{-1}) at 1.0 A·g^{-1} even after 1000 cycles. This advanced electrochemical property is due to its seaweed-liked feature which can bring in plentiful active sites, ameliorate the stresses arisen from volume variations and increase charge transfer rate.

Keywords: WS$_2$/rGO composites; seaweed-liked structure; anode; ultralong cycling life; Lithium ion batteries

1. Introduction

Lithium ion battery, as a green energy storage device, is the alternative to current batteries most potential (for example, shows advanced energy density, which is about 4 times higher than nickel-cadmium battery and 1.6 times higher than nickel-metal hydride battery) [1–3]. However, the ever-lasting need for powerful energy storage equipment, especially for emerging industry (such as electric vehicle and smart grid), has spurred the evolution of the electrode material for LIBs [4–7]. Recently, tremendous researches are focus on transition metal oxides (TMOs) attributing to their highly specific capacity (almost 3 or 4 times higher than graphite). Nonetheless, the practical application of TMOs are hampered by their intrinsic property (e.g., poor ion conductivity, and low structural stability origin from the conversion reaction mechanism). To address these issues, two-dimensional (2D) inorganic transition metal dichalcogenides (TMDs) have been introduced, ascribing to their relative high electronic conductivity, superior specific capacity, marvelous structural stability and environment benignity [8–15].

Tungsten disulfide (WS$_2$), as an important component of the TMDs, has drawn extensive attention owing to its superior theoretical capacity and abundant reserves [16–20]. WS$_2$ is a hexagonal crystal

system, and the underlying crystal structure of WS_2 is composed of three atomic layers connected by van der Waals forces, stacked in the manner of S–W–S, providing the channel for Li^+ ions to be embedded and released [21–25]. Moreover, the large spacing of the WS_2 adjacent layers is more favorable to the transport and the accumulation of lithium ions, which leads to the fact that the geometric structure of the WS_2 can be preserved without an apparent variation during the corresponding electrochemical reaction [26–28]. However, the large-scale commercial application of WS_2 has been impeded by the intrinsic properties of WS_2, including weak electrical conductivity and volume expansion [12,29,30]. The intrinsic properties can cause the collapse of geometrical configuration in cycling processes, followed by a dramatic performance reduction. In this case, enhancing the conductivity of WS_2 and improving structural stability are a potential approach to overcome these obstacles. Several reports have showed that combining WS_2 with the conductive matrix is a promising means to enhance the electrochemical properties, as well as a potential way to alleviate the large volume expansion of the active material [28,31–33]. Graphene is a perfect compound material with advanced electrochemical characteristics and mechanical strength [34]. Li et al. successfully fabricated multi-slices WS_2/rGO nanocomposites by hydrothermal synthesis method [35]. The composite could exhibit a capacity of ~337 $mAh \cdot g^{-1}$ at 2.0 $A \cdot g^{-1}$ after 100 cycles. In addition, multitudinous other various conductive matrix materials have been applied to address these limitations. Ren et al. reported the foam structure WS_2/single-wall carbon nanotube nanocomposites delivers a reversible capacity (~688 $mAh \cdot g^{-1}$) for 1000 cycles at 0.1 $A \cdot g^{-1}$ [36]. Wu et al. designed WS_2/carbon nanofiber composites via combining hydrothermal and electrospinning methods with the presence of a capacity of 545 $mAh \cdot g^{-1}$ at 0.5 $A \cdot g^{-1}$ [37], while Kong et al. prepared WS_2/graphitic carbon nanotubes through combining electrospinning and chemical vapor deposition (CVD) with 570 $mAh \cdot g^{-1}$ at 0.2 $A \cdot g^{-1}$ [38]. Unfortunately, a variety of WS_2 nanocomposites above have been synthesized for LIBs, either the preparation method is too complicated for large-scale production, or the long preparation period increases the production cost, or the cycling performance is slightly insufficient, hindering their further commercial application.

　　　Herein, for higher energy density and a high-rate capability, we synthesized a seaweed-liked WS_2/rGO nanocomposites through a procedure involving the self-assembling of WO_4^{2-}, hexadecyl trimethyl ammonium ion with GO and the subsequent thermal treatment. The seaweed-liked WS_2/rGO nanocomposites, as an anode material, displays an ultralong cycling life and striking rate performance, it can provide a prominent reversible capacity of 507.7 $mAh \cdot g^{-1}$ after 1000 cycles at 1.0 $A \cdot g^{-1}$ and a specific capacity of 108 $mAh \cdot g^{-1}$ at 20.0 $A \cdot g^{-1}$, which shows a highly attractive as the electrode to next-generation LIBs.

2. Experimental

2.1. Preparation of Graphene Oxide (GO)

　　　GO was prepared from flake graphite (325 meshes) via a modified Hummers' method. Under the condition of ice bath, $NaNO_3$ (2.5 g) and flake graphite (2.0 g) were added to 180 mL of concentrated sulphuric acid (H_2SO_4, 95%) while stirring. Subsequently, $KMnO_4$ (15.0 g) was slowly added, and the temperature of the reaction in the process was controlled below 20 °C. Then, 180 mL of DI water was introduced after reaction for 24 h. Next, raise the temperature to 98 °C and maintain for ~1 h. When the temperature dropped to 70 °C, 80 mL of hydrogen peroxide aqueous solution (H_2O_2, 35%) was added. Continue to stir for 1 h after cooling to room temperature. Ultimately, the acquired GO was centrifuged several times with 5% dilute hydrochloric acid and DI water, and then freeze-dried for preservation. The resistance of the deionized (DI) water used for the reaction was ~18 $M\Omega\ cm^{-1}$.

2.2. Synthesis of WS_2/rGO Composites

　　　To fabricate WS_2/rGO composite, GO (40 mg), cetyltrimethyl ammonium bromide (CTAB) (0.364 g), ammonium tungstate (0.5 g) and thiourea (1.83 g) were subsequently dispersed in 25

mL DI water with violent stirring. After freeze-dried, the resulting mixture was heated to 500 °C and kept in an Ar flowing tube furnace for 3 h. The synthesis approach for bare WS_2 were the same as the above composite without the addition of GO.

### 2.3. Characterization Measurements

The obtained samples were analyzed by the scanning electron microscope (SEM, Hitachi S5500, Hitachi, Tokyo, Japan); the field emission transmission electron microscope (FETEM, JEM-2100F, JEOL, Tokyo, Japan); the X-ray photoelectron spectroscopy (XPS, Thermo Escalab 250, Thermo Fisher Scientific, Waltham, United States) with a focused monochromatic Al Kα X-ray source (1486 eV); X-ray diffraction (XRD) patterns (Rigaku MiniFlex 600 X-ray diffractometer, Rigaku, Tokyo, Japan) with Cu Kα (λKα = 1.5406 Å) as the radiation source, and laser confocal Raman microspectroscopy (Raman, Horiba Jobin-Yvon LabRAM HR800, Horiba Jobin-Yvon, Paris, France). The electrochemical impedance spectroscopy (EIS) were measured on a CHI660E (CH instrument, Shanghai, China) in the frequency range of 100 kHz to 0.01 Hz, with an amplitude of 10 mV.

2.4. Electrochemical Measurements

The resulting sample is assembled into the CR 2025 coin-type half cells in a glove box at Ar atmosphere for electrochemical performance testing. 1 M $LiPF_6$ solution (EC/EMC/DEC = 1:1:1 v/v) as the electrolyte, Celgard 2400 membrane as the separator and the lithium metal as the counter/reference electrode. The working electrodes were made of the resulting sample (80 wt%), acetylene black (10 wt%) and polyvinylidene fluoride (10 wt%) dissolved in N-methyl-2-pyrrolidinone to form slurry. The obtained homogeneous paste were pasted on Cu foils with a thickness of ~20 μm and dried in vacuum oven at 90 °C for 12 h and then cut into a wafer with a diameter of 12 mm, each wafer possesses about 1.9 mg active material. The cyclic voltammetry (CV) (CHI660E electrochemical workstation) and galvanostatic charge/discharge cycles (Arbin battery test system, current rate = $(0.1 - 20.0 \text{ A·g}^{-1})$) were tested within the 3.0–0.01 V voltage range. The electrochemical impedance spectroscopy (EIS) were measured on a CHI660E in the frequency range of 10^5 Hz to 10^{-2} Hz, with an amplitude of 10 mV.

3. Results and Discussion

The morphological characteristics of the two prepared nanomaterials were researched by observing the images of SEM and TEM (Figure 1). The WS_2/rGO nanocomposites was fabricated with a procedure involving the self-assembling of $WO_4{}^{2-}$, CTA^+ with GO and the subsequent thermal treatment. The obtained WS_2/rGO sample exhibits a uniform seaweed-liked morphology in Figure 1b. There is no sight of nanosheets from rGO. Since CTA^+ facilitates to reduce the innate charge incompatibility between negatively charged GO and $WO_4{}^{2-}$, ascribing to the electrostatic interaction, there is no conspicuous interfacial structure between rGO and WS_2 (synthesis from the subsequent calcination with the presence of thiourea) in Figure 1c. The high magnification of WS_2/rGO can be seen in Figure 1c. In contrast, the bare WS_2 without GO just form short rod shape in Figure 1a, which illustrates that GO plays an indispensable role in the production of the seaweed-liked nanostructures. To further investigate the structure of WS_2/rGO nanocomposite, Figure 1d displays the TEM images of WS_2/rGO nanocomposite. The spacing of the clear lattice fringe is 0.65 nm, corresponding to the d-spacing of (002) plane of the c-axis of hexagonal WS_2. The thin rGO is attached to the surface of the few layer WS_2 nanosheets as shown in Figure 1d. The added GO is reduced to rGO during the calcining phase and formed stable seaweed-liked composite with WS_2, not only providing an efficient conductive path for electron transport, but also avoiding a structure collapse of the electrode, owing to the huge volume expansion. Which is consistent with the XRD patterns shown in Figure 2a.
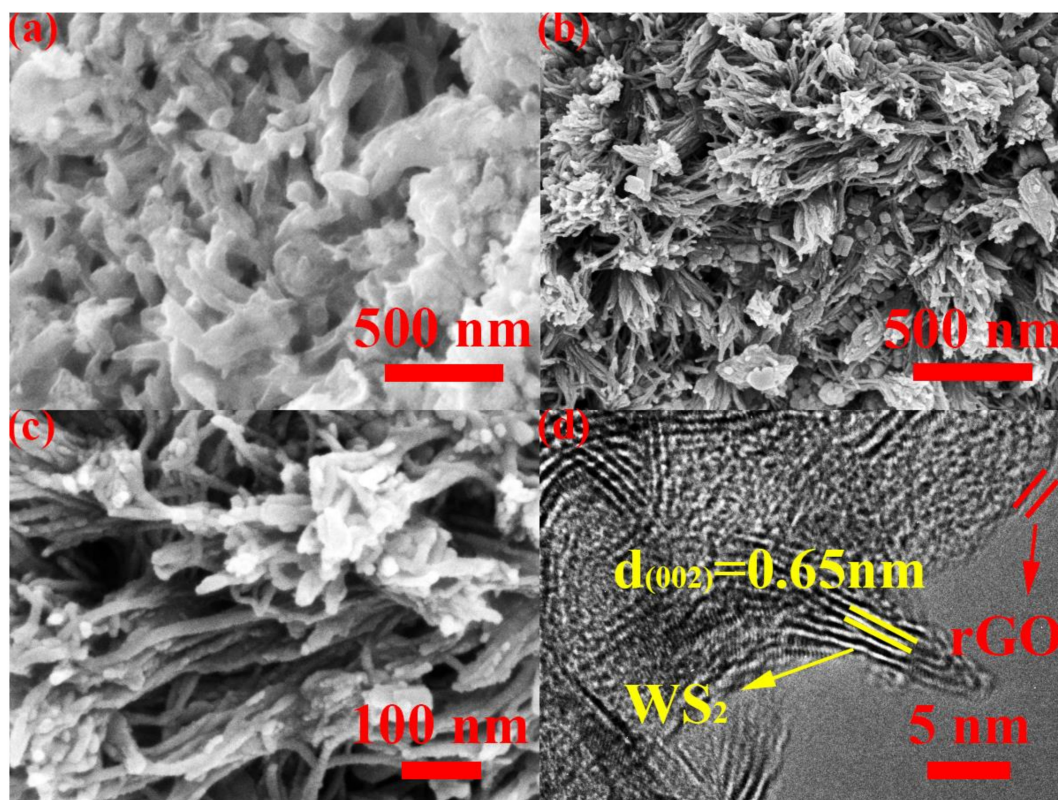
Figure 1. (**a**) SEM images of bare WS_2 and (**b**–**c**) SEM, (**d**) TEM images of WS_2/rGO composites.

Figure 2a shows X-ray diffraction patterns of the two samples. All conspicuous diffraction peaks (at 2θ = 13.52°, 33.81°, 59.28°) can be easily linked to the 2H-WS_2 without the existence of other phases or impurities, demonstrating the high purity of the obtained WS_2 (Figure 2a). Furthermore, a few-layered structure of WS_2 can be certified by the presence of (002), (100) and (110) reflections. Since the existence of the rGO diminishes the intensity of incoming and reflected X-ray light, the reduction of the diffraction peaks intensity of WS_2/rGO can be clearly observed. The similar attenuation also can be observed in Raman spectra (Figure 2b), where the intensity of the characteristic Raman signature of WS_2 (located at 346 and 409 cm^{-1} correspond to the E_{2g} and A_{1g} modes, respectively) in WS_2/rGO shows obviously weaker than that of bare WS_2. Moreover, Raman spectrum of WS_2/rGO shown in Figure 2b also can certify the existence of rGO attributing the emergence of two prominent peaks D (relate to the symmetric k-point phonon pattern of A_{1g}) and G (ascribing to the E_{2g} phonon of C sp^2 atoms).
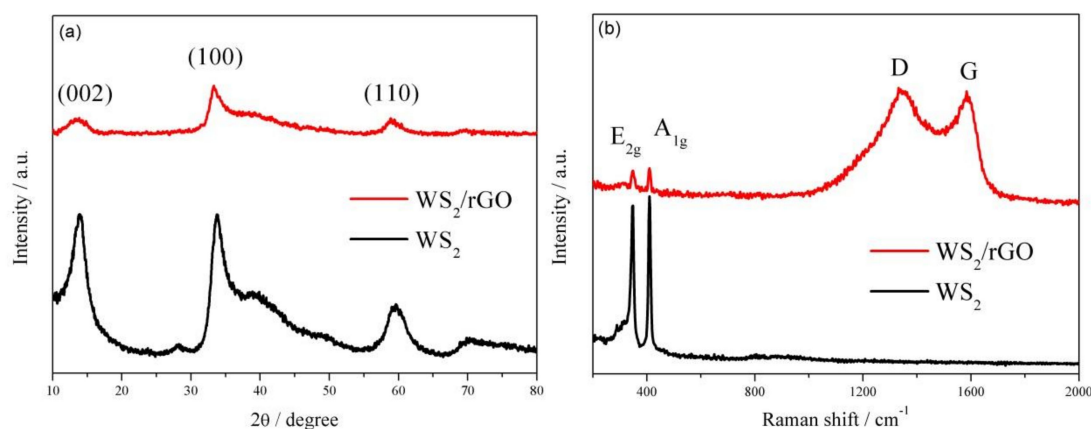

Figure 2. (**a**) XRD patterns and (**b**) Raman spectra of WS_2 and WS_2/rGO.

XPS analyses were applied to identify the chemical composition of the WS_2/rGO sample (Figure 3). The presence of W, S, C and O (originate from the unreduced oxygeneous groups of the rGO) in the WS_2/rGO composite is certified by survey spectrum shown in Figure 3a. The distribution of the W 4f peaks on WS_2 can be testified through two obviously peaks at 34.9 and 32.7 eV (in Figure 3b), corresponding to the W $4f_{5/2}$ and W $4f_{7/2}$ spin peaks of WS_2, respectively. Meanwhile, the high-resolution spectrum of S (Figure 3c) illustrates two characteristic peaks at 162.0 and 163.0 eV that stemmed from the S^{2-} typical of WS_2. The high-resolution spectral of C 1s is presented in Figure 3d, where three different components (in 287.8, 284.8 and 284.1 eV) can be observed, corresponding to the C=O, C–O and C–C bonds of rGO, respectively, which in line with the previously reports [39–41].
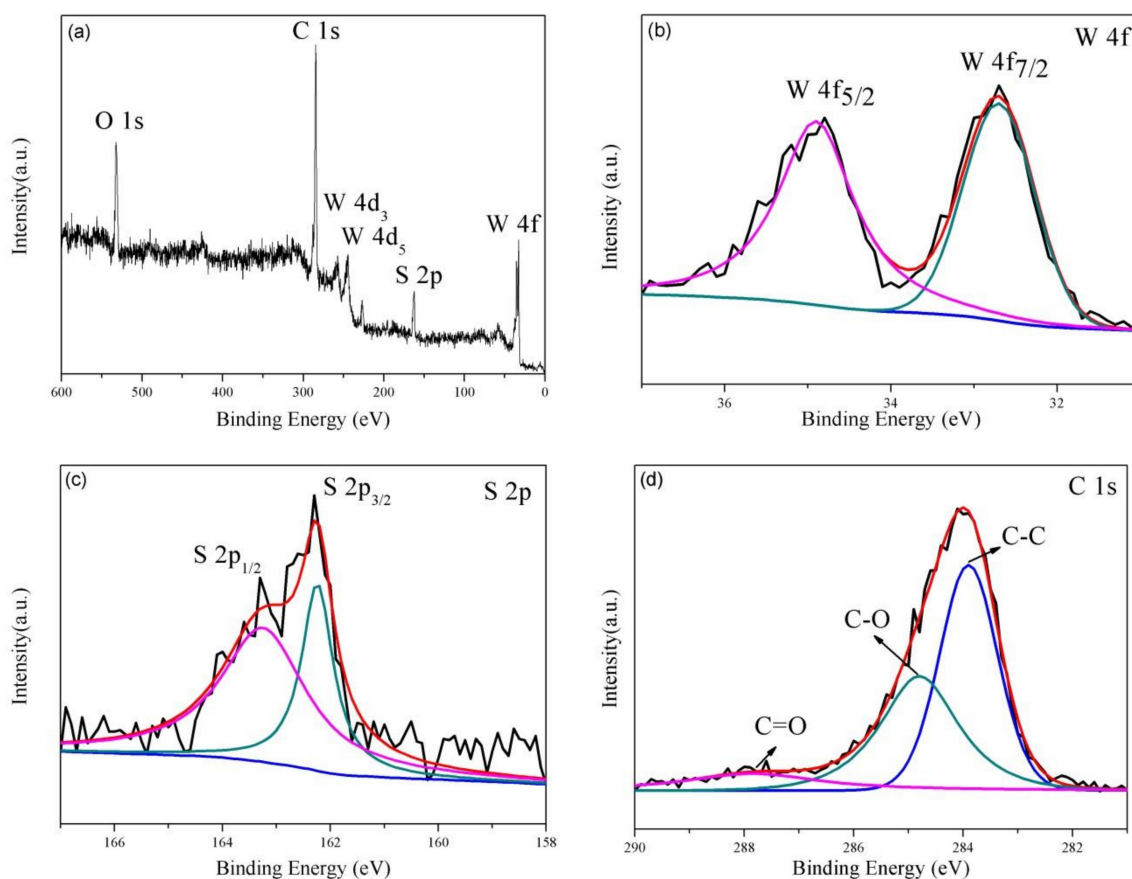
Figure 3. (**a**) broad XPS scan spectrum of WS_2/rGO composites; the high-resolution spectrum of (**b**) W 4f; (**c**) S 2p; (**d**) C 1s.

The electrochemical process of the WS_2/rGO composite electrode in charge-discharge cycling was investigated by the initial six cycles cyclic voltammogram (CV) at 0.01 mV·s^{-1} in Figure 4a. As shown in Figure 4a, the reduction peak at 1.65 V and oxidation peak at 2.35 V can be observed clearly in the first cycle, which was caused by the insertion/extraction reaction of Li$^+$ in the WS_2 interlayer space ($WS_2 + xLi^+ + xe^- \leftrightarrow Li_xWS_2$). Another obvious reduction peak can be seen at 0.45 V that arises from the reduction of WS_2 ($WS_2 + 4Li^+ + 4e^- \rightarrow W + 2Li_2S$), and accompanying by non-aqueous electrolyte decomposition and adverse reactions between Li$^+$ and the residual oxygen-containing functional groups. In the second cycle onwards, reduction peaks at 1.65 and 0.45 V no longer can be observed, meanwhile, a new reaction at 1.75–2.18 V can be visualized. This change could be accounted by the production of gel-liked solid electrolyte interphase (SEI) film [42]. Moreover, those cyclic voltammograms were nearly fully superimposable, indicating the excellent reversibility and cycle stability of the WS_2/rGO nanocomposites.
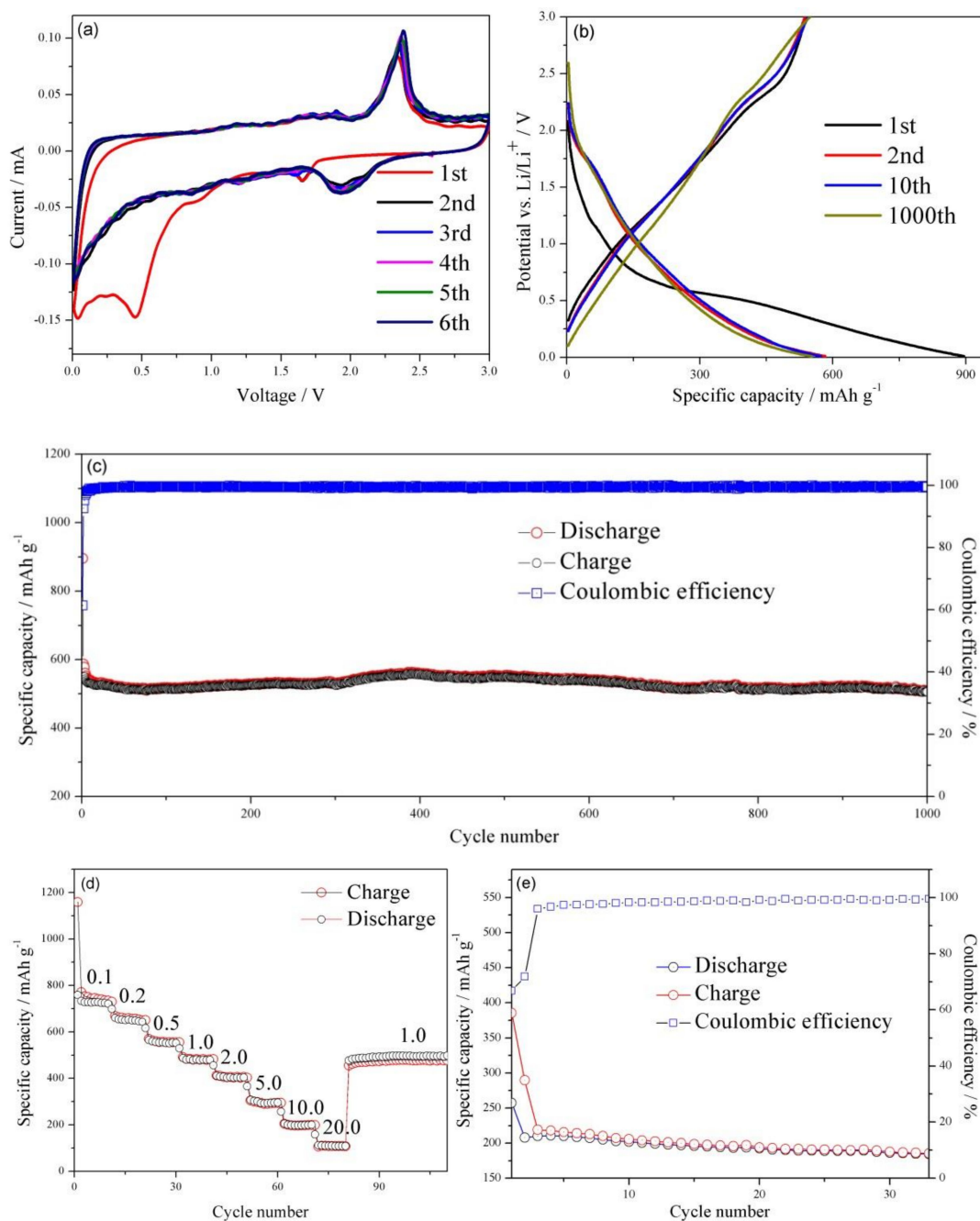
Figure 4. (**a**) CV curves of the WS_2/rGO composite at 0.01 $mV \cdot s^{-1}$ in the 0.01 to 3.0 V voltage window. (**b**) Charge/discharge voltage profiles of WS_2/rGO at 1.0 $A \cdot g^{-1}$. (**c**) The cycle stabilities of the WS_2/rGO at 1.0 $A \cdot g^{-1}$. (**d**) The rate capacities of WS_2/rGO at 0.1, 0.2, 0.5, 1.0, 2.0, 5.0, 10.0 and 20.0 $A \cdot g^{-1}$. (**e**) The cycle stabilities of the bare WS_2 at 1.0 $A \cdot g^{-1}$.

Figure 4b illustrates the charge-discharge curves of WS_2/rGO material at 1st, 2nd, 100th and 1000th cycles under 1.0 $A \cdot g^{-1}$, respectively. The voltage plateau appears in the first discharge curve around 0.55 V, which may be ascribed to WS_2 being reduced to metallic W at the same time that Li_2O is generated. The first discharge/charge capacity of the WS_2/rGO composites comes to 895.8 $mAh \cdot g^{-1}$ and 546.3 $mAh \cdot g^{-1}$, causing a high premier Coulombic efficiency of 60.9%. The nonreversible loss of the first cycle is probably ascribed to the adverse reactions between Li^+ and the residual oxygen-containing functional groups on the WS_2/rGO composites, and the formation of SEI film during lithium ion intercalation process [43–47], which makes the following discharge curves exhibit a totally different voltage plateau at 2.0 V, in conformity to the aforementioned CV curves, suggesting the superior

electrochemical property of the WS_2/rGO composites. This was also explained by the similarity between the 2nd, the 10th and the 1000th charge/discharge profiles of the WS_2/rGO (Figure 4b) and their near coulombic efficiency after the first several cycles in Figure 4c. Furthermore, the WS_2/rGO composites electrodes present a marvelous cycle stability at 1.0 $A\cdot g^{-1}$ (Figure 4c). Even after 1000th cycle, the WS_2/rGO composites electrode still have a charge capacities of 505.6 $mAh\cdot g^{-1}$ and a discharge capacities of 507.7 $mAh\cdot g^{-1}$. Compared with the capacities of another WS_2-based anode materials report previously, the stable reversible capacity of the WS_2/rGO composites is much higher, suggesting the superiority of using the WS_2/rGO composites as an anode material for LIBs [12].

To further study the advanced electrochemical characteristics of the WS_2/rGO composites electrode, rate capability also has been evaluated (Figure 4d). As the current density increases from 0.1 to 0.2, 0.5, 1.0, 2.0 and 5.0 $A\cdot g^{-1}$, the different discharged capacities of 720, 650, 554, 479, 402 and 300 $mAh\cdot g^{-1}$ are delivered, respectively. The reversible capacities of the WS_2/rGO electrode with 199 and 108 $mAh\cdot g^{-1}$ still can be achieved while the current density increases to 10.0 and 20.0 $A\cdot g^{-1}$, respectively. Significantly, after returning to 1.0 $A\cdot g^{-1}$, the capacity of WS_2/rGO composites immediately recovered to 508.5 mAh^{-1}, demonstrating the excellent electrode conductivity and fast Li^+ diffusion.

For in-depth reveal the role of rGO in the WS_2/rGO electrode, the circulation property of the bare WS_2 electrode has been assessed. The capacity of bare WS_2 is only ~200 $mAh\cdot g^{-1}$ in Figure 4e, far lower than that of the WS_2/rGO composites. In addition, the bare WS_2 electrode suffers a sustaining capacity fading after the first few cycles, manifesting the prominent cycling property of the WS_2/rGO on the side. The result is consistent with the conclusion of the morphology of the two materials in Figures 1a and 1b. The rGO is formed stable seaweed-liked composite with WS_2, avoiding a structure collapse of the electrode owing to the huge volume expansion and providing a highly conductive path for electron transport. Besides, the seaweed-liked structure materials will provide much more active sites, ameliorate the stresses arisen from volume variations and increase charge transfer rate to further improve lithium storage capacity and ionic conductivity [48].

An EIS measurement was conducted for two samples to further research the electrochemical behavior in Figure 5. The tests in this survey were achieved after 100 cycles. Generally, the impedance spectra was composed of semicircle and a skew line, which were related to the charge transfer resistance and ion diffusion process, respectively [46]. It can be seen that the semicircle size of the WS_2/rGO is much smaller than that of the bare WS_2. The Rs and Rc of the bare WS_2 and the WS_2/rGO composites can be extracted by using equivalent circuit shown in the inset of Figure 5, which are 20.9, 116.4, 7.2 and 27.5 Ω, respectively, suggesting the faster charge transfer speed of WS_2/rGO. Therefore, the addition of rGO can effectively enhance the conductivity performance of WS_2 and greatly decrease charge transfer resistance, which is consistent with the expectation.
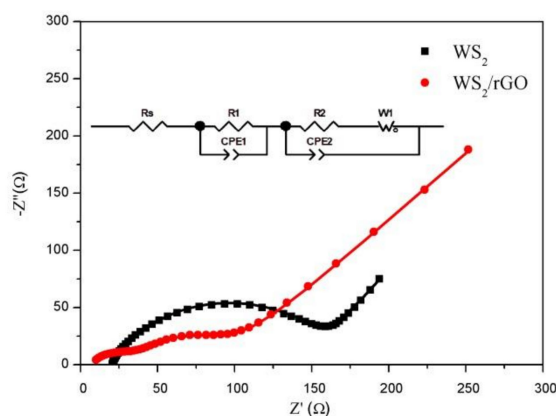
Figure 5. The Nyquist plots of bare WS_2 and WS_2/rGO composite range from 10^5 Hz to 10^{-2} Hz after 100 cycles.

4. Conclusions

In summary, the seaweed-liked WS_2/rGO nanocomposites was fabricated by a procedure involving the self-assembling of WO_4^{2-}, CTA^+ with GO and the subsequent thermal treatment. The WS_2/rGO material as the anode material for LIBs exhibited ultralong cycling life and striking rate performance with a stable and remarkable capacity of 507.7 mAh·g^{-1} at 1.0 A·g^{-1} after 1000 cycles. Furthermore, it was worth nothing that its capacities of 108 mAh·g^{-1} could still be maintained while the current density increases to 20.0 A·g^{-1}. Noteworthily, after returning to 1.0 A·g^{-1}, the capacity of WS_2/rGO composites immediately recovered to 508.5 mAh^{-1}. The superior electrochemical property could depend on the synergy of WO_4^{2-}, CTA^+ and GO. The added GO is reduced to rGO during the calcining phase and formed stable seaweed-liked composite with WS_2, not only providing an efficient conductive path for electron transport, but also avoiding a structure collapse of the electrode owing to the huge volume expansion. Moreover, the seaweed-liked structure would provide much more active sites, ameliorate the stresses arisen from volume variations and increase charge transfer rate to further improve lithium storage capacity and ionic conductivity. The seaweed-liked WS_2/rGO nanocomposites show great promise for other energy storage devices (e.g., sodium-ion battery).

Author Contributions: Conceptualization, X.Y. and H.T.; methodology, Y.J. and X.Y.; formal analysis, X.Z., X.D. and W.X.; resources, Y.Z. and X.Y.; data curation, Y.H. and Y.J.; writing-original draft preparation, Y.H. and Y.J.; writing-review & editing, Z.M., Y.J. and X.Y.

Conflicts of Interest: The authors declare no conflict of interest.

References

1.   Youn, D.H.; Jo, C.; Kim, J.Y.; Lee, J.; Lee, J.S. Ultrafast synthesis of MoS_2 or WS_2-reduced graphene oxide composites via hybrid microwave annealing for anode materials of lithium ion batteries. *J. Power Sources* **2015**, *295*, 228–234. [CrossRef]

2.   Xu, D.; Mu, C.; Xiang, J.; Wen, F.; Su, C.; Hao, C.; Hu, W.; Tang, Y.; Liu, Z. Carbon-encapsulated Co_3O_4@CoO@Co nanocomposites for multifunctional applications in enhanced long-life lithium storage, supercapacitor and oxygen evolution reaction. *Electrochim. Acta* **2016**, *220*, 322–330. [CrossRef]

3.   Wu, Q.; Zhao, R.; Liu, W.; Zhang, X.; Shen, X.; Li, W.; Diao, G.; Chen, M. In-depth nanocrystallization enhanced Li-ions batteries performance with nitrogen-doped carbon coated Fe_3O_4 yolk−shell nanocapsules. *J. Power Sources* **2017**, *344*, 74–84. [CrossRef]

4.   Raccichini, R.; Varzi, A.; Passerini, S.; Scrosati, B. The role of graphene for electrochemical energy storage. *Nat. Mater.* **2015**, *14*, 271. [CrossRef]

5.   Li, X.; Feng, Z.; Zai, J.; Ma, Z.-F.; Qian, X. Incorporation of Co into MoS_2/graphene nanocomposites: One effective way to enhance the cycling stability of Li/Na storage. *J. Power Sources* **2018**, *373*, 103–109. [CrossRef]

6.   Schwieters, T.; Evertz, M.; Mense, M.; Winter, M.; Nowak, S. Lithium loss in the solid electrolyte interphase: Lithium quantification of aged lithium ion battery graphite electrodes by means of laser ablation inductively coupled plasma mass spectrometry and inductively coupled plasma optical emission spectroscopy. *J. Power Sources* **2017**, *356*, 47–55. [CrossRef]

7.   Yoon, Y.H.; Kim, D.S.; Kim, M.; Park, M.S.; Lee, Y.-C.; Kim, K.H.; Kim, I.T.; Hur, J.; Lee, S.G. Investigation of electrochemical performance on carbon supported tin-selenium bimetallic anodes in lithium-ion batteries. *Electrochim. Acta* **2018**, *266*, 193–201. [CrossRef]

8.   Zhang, X.; Zhao, R.; Wu, Q.; Li, W.; Shen, C.; Ni, L.; Yan, H.; Diao, G.; Chen, M. Petal-like MoS_2 nanosheets space-confined in hollow mesoporous carbon spheres for enhanced lithium storage performance. *ACS Nano* **2017**, *11*, 8429–8436. [CrossRef]

9.   Yuan, Z.; Jiang, Q.; Feng, C.; Chen, X.; Guo, Z. Synthesis and Performance of Tungsten Disulfide/Carbon (WS_2/C) Composite as Anode Material. *J. Electron. Mater.* **2018**, *47*, 251–260. [CrossRef]

10. Stephenson, T.; Li, Z.; Olsen, B.; Mitlin, D. Lithium ion battery applications of molybdenum disulfide (MoS_2) nanocomposites. *Energy Environ. Sci.* **2014**, *7*, 209–231. [CrossRef]

11. Cao, X.; Tan, C.; Zhang, X.; Zhao, W.; Zhang, H. Solution-Processed Two-Dimensional Metal Dichalcogenide-Based Nanomaterials for Energy Storage and Conversion. *Adv. Mater.* **2016**, *28*, 6167–6196. [CrossRef] [PubMed]

12. Yu, X.; Pei, C.; Chen, W.; Feng, L. 2 dimensional WS_2 tailored nitrogen-doped carbon nanofiber as a highly pseudocapacitive anode material for lithium-ion battery. *Electrochim. Acta* **2018**, *272*, 119–126. [CrossRef]

13. Zhang, Z.; Wu, S.; Cheng, J.; Zhang, W. MoS_2 nanobelts with (002) plane edges-enriched flat surfaces for high-rate sodium and lithium storage. *Energy Storage Mater.* **2018**, *15*, 65–74. [CrossRef]

14. Minakshi, M.; Mitchell, D.R.; Baur, C.; Chable, J.; Barlow, A.J.; Fichtner, M.; Banerjee, A.; Chakraborty, S.; Ahuja, R. Phase evolution in calcium molybdate nanoparticles as a function of synthesis temperature and its electrochemical effect on energy storage. *Nanoscale Adv.* **2019**, *1*, 565–580. [CrossRef]

15. Manickam, M.; David, M.; Reddy, M.A.; Barlow, A.J.; Maximilian, F. New insights into the electrochemistry of magnesium molybdate hierarchical architectures for high performance sodium devices. *Nanoscale* **2018**, *10*, 13277–13288.

16. Hussain, S.; Patil, S.A.; Memon, A.A.; Vikraman, D.; Naqvi, B.A.; Jeong, S.H.; Kim, H.-S.; Kim, H.-S.; Jung, J. CuS/WS_2 and CuS/MoS_2 heterostructures for high performance counter electrodes in dye-sensitized solar cells. *Sol. Energy* **2018**, *171*, 122–129. [CrossRef]

17. Kumar, K.S.; Choudhary, N.; Jung, Y.; Thomas, J. Recent advances in two-dimensional nanomaterials for supercapacitor electrode applications. *ACS Energy Lett.* **2018**, *3*, 482–495. [CrossRef]

18. Lin, T.W.; Sadhasivam, T.; Wang, A.Y.; Chen, T.Y.; Lin, J.Y.; Shao, L.D. Ternary Composite Nanosheets with $MoS_2/WS_2/Graphene$ Heterostructures as High-Performance Cathode Materials for Supercapacitors. *ChemElectroChem* **2018**, *5*, 1024–1031. [CrossRef]

19. Zhu, M.; Zhai, C.; Fujitsuka, M.; Majima, T. Noble metal-free near-infrared-driven photocatalyst for hydrogen production based on 2D hybrid of black Phosphorus/WS_2. *Appl. Catal. B Environ.* **2018**, *221*, 645–651. [CrossRef]

20. Li, T.; Guo, R.; Luo, Y.; Li, F.; Liu, Z.; Meng, L.; Yang, Z.; Luo, H.; Wan, Y. Innovative N-doped graphene-coated WS_2 nanosheets on graphene hollow spheres anode with double-sided protective structure for Li-Ion storage. *Electrochim. Acta* **2018**, *290*, 128–141. [CrossRef]

21. Yang, D.; Frindt, R. Li-intercalation and exfoliation of WS_2. *J. Phys. Chem. Solids* **1996**, *57*, 1113–1116. [CrossRef]

22. Yebka, B.; Julien, C. Studies of lithium intercalation in 3R-WS_2. *Solid State Ion.* **1996**, *90*, 141–149. [CrossRef]

23. Chhowalla, M.; Shin, H.S.; Eda, G.; Li, L.-J.; Loh, K.P.; Zhang, H. The chemistry of two-dimensional layered transition metal dichalcogenide nanosheets. *Nat. Chem.* **2013**, *5*, 263. [CrossRef] [PubMed]

24. Voiry, D.; Yamaguchi, H.; Li, J.; Silva, R.; Alves, D.C.; Fujita, T.; Chen, M.; Asefa, T.; Shenoy, V.B.; Eda, G. Enhanced catalytic activity in strained chemically exfoliated WS_2 nanosheets for hydrogen evolution. *Nat. Mater.* **2013**, *12*, 850. [CrossRef] [PubMed]

25. Kumar, A.; Ahluwalia, P. Electronic transport and dielectric properties of low-dimensional structures of layered transition metal dichalcogenides. *J. Alloys Compd.* **2014**, *587*, 459–467. [CrossRef]

26. Feng, C.; Ma, J.; Li, H.; Zeng, R.; Guo, Z.; Liu, H. Synthesis of molybdenum disulfide (MoS_2) for lithium ion battery applications. *Mater. Res. Bull.* **2009**, *44*, 1811–1815. [CrossRef]

27. Chen, D.; Ji, G.; Ding, B.; Ma, Y.; Qu, B.; Chen, W.; Lee, J.Y. In situ nitrogenated graphene—Few-layer WS_2 composites for fast and reversible Li^+ storage. *Nanoscale* **2013**, *5*, 7890–7896. [CrossRef]

28. Li, X.; Zhang, J.; Liu, Z.; Fu, C.; Niu, C. WS_2 nanoflowers on carbon nanotube vines with enhanced electrochemical performances for lithium and sodium-ion batteries. *J. Alloys Compd.* **2018**, *766*, 656–662. [CrossRef]

29. Zeng, X.; Ding, Z.; Ma, C.; Wu, L.; Liu, J.; Chen, L.; Ivey, D.G.; Wei, W. Hierarchical nanocomposite of hollow N-doped carbon spheres decorated with ultrathin WS_2 nanosheets for high-performance lithium-ion battery anode. *ACS Appl. Mater. Interfaces* **2016**, *8*, 18841–18848. [CrossRef]

30. Ansari, M.Z.; Ansari, S.A.; Parveen, N.; Cho, M.H.; Song, T. Lithium ion storage ability, supercapacitor electrode performance, and photocatalytic performance of tungsten disulfide nanosheets. *New J. Chem.* **2018**, *42*, 5859–5867. [CrossRef]

31. Gao, P.; Yang, Z.; Liu, G.; Qiao, Q. Facile synthesis of MoS$_2$/MWNT anode material for high-performance lithium-ion batteries. *Ceram. Int.* **2015**, *41*, 1921–1925. [CrossRef]

32. Pang, Q.; Gao, Y.; Zhao, Y.; Ju, Y.; Qiu, H.; Wei, Y.; Liu, B.; Zou, B.; Du, F.; Chen, G. Improved Lithium-Ion and Sodium-Ion Storage Properties from Few-Layered WS$_2$ Nanosheets Embedded in a Mesoporous CMK-3 Matrix. *Chem. Eur. J.* **2017**, *23*, 7074–7080. [CrossRef]

33. Liu, H.; Huang, Z.; Wu, G.; Wu, Y.; Yuan, G.; He, C.; Qi, X.; Zhong, J. A novel WS$_2$/NbSe$_2$ vdW heterostructure as an ultrafast charging and discharging anode material for lithium-ion batteries. *J. Mater. Chem. A* **2018**, *6*, 17040–17048. [CrossRef]

34. Nandi, D.K.; Sen, U.K.; Choudhury, D.; Mitra, S.; Sarkar, S.K. Atomic layer deposited MoS$_2$ as a carbon and binder free anode in Li-ion battery. *Electrochim. Acta* **2014**, *146*, 706–713. [CrossRef]

35. Li, H.; Yu, K.; Fu, H.; Guo, B.; Lei, X.; Zhu, Z. Multi-slice nanostructured WS$_2$@rGO with enhanced Li-ion battery performance and a comprehensive mechanistic investigation. *Phys. Chem. Chem. Phys.* **2015**, *17*, 29824–29833. [CrossRef]

36. Ren, J.; Wang, Z.; Yang, F.; Ren, R.-P.; Lv, Y.-K. Freestanding 3D single-wall carbon nanotubes/WS$_2$ nanosheets foams as ultra-long-life anodes for rechargeable lithium ion batteries. *Electrochim. Acta* **2018**, *267*, 133–140. [CrossRef]

37. Wu, C.; Zeng, X.; He, P.; Chen, L.; Wei, W. Flexible WS$_2$@CNFs Membrane Electrode with Outstanding Lithium Storage Performance Derived from Capacitive Behavior. *Adv. Mater. Interfaces* **2018**, *5*, 1701080. [CrossRef]

38. Kong, D.; Qiu, X.; Wang, B.; Xiao, Z.; Zhang, X.; Guo, R.; Gao, Y.; Yang, Q.-H.; Zhi, L. WS$_2$ nanoplates embedded in graphitic carbon nanotubes with excellent electrochemical performance for lithium and sodium storage. *Sci. China Mater.* **2018**, *61*, 671–678. [CrossRef]

39. Jiang, Z.; Jiang, Z.-J.; Maiyalagan, T.; Manthiram, A. Cobalt oxide-coated N-and B-doped graphene hollow spheres as bifunctional electrocatalysts for oxygen reduction and oxygen evolution reactions. *J. Mater. Chem. A* **2016**, *4*, 5877–5889. [CrossRef]

40. Ramkumar, R.; Sundaram, M.M. A biopolymer gel-decorated cobalt molybdate nanowafer: Effective graft polymer cross-linked with an organic acid for better energy storage. *New J. Chem.* **2016**, *40*, 2863–2877. [CrossRef]

41. Jiang, Y.; Yan, X.; Xiao, W.; Tian, M.; Gao, L.; Qu, D.; Tang, H. Co$_3$O$_4$-graphene nanoflowers as anode for advanced lithium ion batteries with enhanced rate capability. *J. Alloys Compd.* **2017**, *710*, 114–120. [CrossRef]

42. Shiva, K.; Matte, H.R.; Rajendra, H.; Bhattacharyya, A.J.; Rao, C. Employing synergistic interactions between few-layer WS$_2$ and reduced graphene oxide to improve lithium storage, cyclability and rate capability of Li-ion batteries. *Nano Energy* **2013**, *2*, 787–793. [CrossRef]

43. Zuniga, L.; Agubra, V.; Flores, D.; Campos, H.; Villareal, J.; Alcoutlabi, M. Multichannel hollow structure for improved electrochemical performance of TiO$_2$/Carbon composite nanofibers as anodes for lithium ion batteries. *J. Alloys Compd.* **2016**, *686*, 733–743. [CrossRef]

44. Agubra, V.A.; Zuniga, L.; Flores, D.; Campos, H.; Villarreal, J.; Alcoutlabi, M. A comparative study on the performance of binary SnO$_2$/NiO/C and Sn/C composite nanofibers as alternative anode materials for lithium ion batteries. *Electrochim. Acta* **2017**, *224*, 608–621. [CrossRef]

45. Huang, X.D.; Zhang, F.; Gan, X.F.; Huang, Q.A.; Tang, W.M. Electrochemical characteristics of amorphous silicon carbide film as a lithium-ion battery anode. *RSC Adv.* **2018**, *8*, 5189–5196. [CrossRef]

46. Sun, X.; Shao, C.; Zhang, F.; Li, Y.; Wu, Q.H.; Yang, Y. SiC Nanofibers as Long-Life Lithium-Ion Battery Anode Materials. *Front. Chem.* **2018**, *6*, 166. [CrossRef] [PubMed]

47. Jiang, Y.; Yan, X.; Mei, P.; Zhang, Y.; Xiao, W.; Tang, H. Electrochemical reconstruction induced high electrochmical performance of Co$_3$O$_4$/reduced graphene oxide for lithium ion batteries. developments in nanostructured anode materials for rechargeable lithium-ion batteries. *J. Alloys Compd.* **2018**, *764*, 80–87. [CrossRef]

48. Ji, L.; Lin, Z.; Alcoutlabi, M.; Zhang, X. Recent developments in nanostructured anode materials for rechargeable lithium-ion batteries. *Energy Environ. Sci.* **2011**, *4*, 2682–2699. [CrossRef]